Measurements of Hot-Electron Temperature in Laser-Irradiated Plasmas

Introduction

Recently published work[1–3] has studied the production of hot electrons related to the two-plasmon–decay (TPD) instability caused by laser pulse interaction with solid planar targets at an irradiation of 10^{14} W/cm^2. The hot electrons generated by TPD can preheat the cold compressed core in cryogenic implosions, thereby degrading the final compression and the target performance.[4–6] The first step in evaluating preheat is to determine the hot-electron temperature (T_{hot}). It is required for (a) deducing the total energy in hot electrons from the measured target x-ray radiation (K$_\alpha$ or continuum), and (b) calculating the hot-electron energy deposition in the fuel, i.e., the preheat. In previous work[1–3] we deduced T_{hot} from the measured hard x-ray (HXR) spectrum using a three-channel fluorescence-photomultiplier hard x-ray detector (HXRD).[7] The total energy in hot electrons (E_{hot}) was derived from the Mo K$_\alpha$ line intensity from an embedded Mo target. We extend those measurements here by

a. implementing a new nine-channel hard x-ray image-plate (HXIP) spectrometer to measure the hot-electron temperature more reliably and to derive the total energy in hot electrons. The spectrum is recorded on image plates (IP's) that are absolutely calibrated;[8] this feature makes it possible to derive E_{hot} (which was not the case with the uncalibrated HXRD, where E_{hot} was derived from K$_\alpha$ measurements). T_{hot} is found to be consistently lower (by a factor of 1.5 to 1.7) than the results reported in Ref. 1.

b. performing experiments to measure T_{hot} independently of the x-ray continuum spectrum (using ratios of K$_\alpha$ lines). The results (see **K$_\alpha$ Measurement of T_{hot}**, p. 138) were consistent with those derived from the continuum spectrum measured by HXIP.

c. measuring the thermal (softer) x-ray spectrum from the heated plasma and including it in the derivation of the total energy in hot electrons from the high-energy continuum.

d. demonstrating that the total energy in hot electrons derived from the measurements of K$_\alpha$ and from the high-energy continuum are consistent.

Determining preheat of fusion targets by hot electrons consists of two stages: (1) determining T_{hot} and then the total energy in hot electrons (or the total number of hot electrons) and (2) determining the energy deposited by the hot electrons in the compressed, cold target core. The second stage is target specific and is not discussed in this article. The first stage yields a quasi-universal curve of the fraction $f_{hot} = E_{hot}/E_L$ of laser energy (E_L) converted to hot electrons. As shown in Ref. 1, f_{hot} for planar targets rises steeply from the TPD threshold at a laser intensity of ~1.5×10^{14} W/cm^2 and then saturates at a value of a few percent above ~7×10^{14} W/cm^2. For spherical targets, the value of f_{hot} at a given laser intensity is smaller than it is for planar targets (because the density scale length is smaller in spherical targets). However, when f_{hot} is plotted as a function of the calculated TPD linear gain (or, alternatively, as a function of the measured T_{hot}), the measured f_{hot} points fall on a quasi-universal curve, independent of the target geometry.[2,3] Therefore, the planar-target measurements in this and previous articles[1–3] are relevant to calculating preheat in spherically imploding fusion targets: the fraction f_{hot} (and the concomitant T_{hot}) serves as a source to calculate the transport of hot electrons through the target at hand.

We used two methods to determine the total energy in hot electrons in our planar-target experiments: (1) the emission of K$_\alpha$ lines from an embedded high-Z target layer and (2) from the high-energy bremsstrahlung emission. The targets must be thick enough to capture most of the hot electrons. The targets in these experiments were either 30-μm-thick Mo or 125-μm-thick CH [the targets discussed in **K$_\alpha$ Measurement of T_{hot}** (p. 138) were for measuring T_{hot}, not E_{hot}, and were thicker]. In each case the range of most electrons is smaller than the target thickness, so most of the hot-electron energy is included. The high-Z targets were coated with a 30-μm-thick CH layer;

therefore, in all cases the laser interacted with CH, and the production of hot electrons was the same for the same laser intensity and target geometry. In the cases of high-Z targets, it was evident that the laser did not burn through the outer CH layer because of the absence of high-Z lines, except for the inner-shell K_α transitions, i.e., lines excited by the hot electrons.

Measuring E_{hot} in implosion experiments is difficult because (a) a high-Z layer cannot be incorporated into the target core without modifying the desired implosion characteristics and (b) the electrons (mostly those that miss the compressed core) lose a small fraction of their energy in making one pass through the target; this requires knowledge of the hot-electron divergence and refluxing back into the target. Cryogenic targets present an additional complication: even if E_{hot} is known, the preheat of the compressed fuel is not simple to derive because most of the HXR radiation is emitted by the CH corona, not the compressed fuel.[9] However, measuring the hot-electron source using thick planar targets makes it possible to calculate the transport of hot electrons through the fusion target at the same TPD gain or the same T_{hot}.

High-Z target layers in the previous work served a different purpose than in the present experiments: in the previous experiments, the high-Z K_α lines were used to determine E_{hot} (while the required T_{hot} came from HXRD, which, being uncalibrated, could not yield E_{hot}). Here, T_{hot} comes from HXIP (i.e., from the continuum slope) as well as from K_α line ratios (in the targets discussed in **K_α Measurement of T_{hot}**, p. 138), whereas E_{hot} also comes from the absolutely calibrated HXIP.

The laser configuration here was the same as in Ref. 1: four OMEGA EP[10] beams intersected the target at an angle of 23° with respect to the target normal. The laser pulse had a square temporal shape with a width of 2 ns. The irradiance was varied in the range of ~1 to 7×10^{14} W/cm² by increasing the laser energy in the range of ~2 to 9 kJ.

The energy in hot electrons (E_{hot}) was derived from either the K_α emission from the high-Z layers or the HXR bremsstrahlung radiation (using the calibrated readings of the HXIP). The relation between the measurements and E_{hot} was calculated using the *EGSnrc* Monte Carlo code.[11] The code assumes, as input, a Maxwellian hot-electron spectrum that is transported through the planar target. Figure 147.22 shows the calculated ratios of hot-electron energy and radiation yield as well as hot-electron energy and K_α emission. The blue curve uses the photostimu-
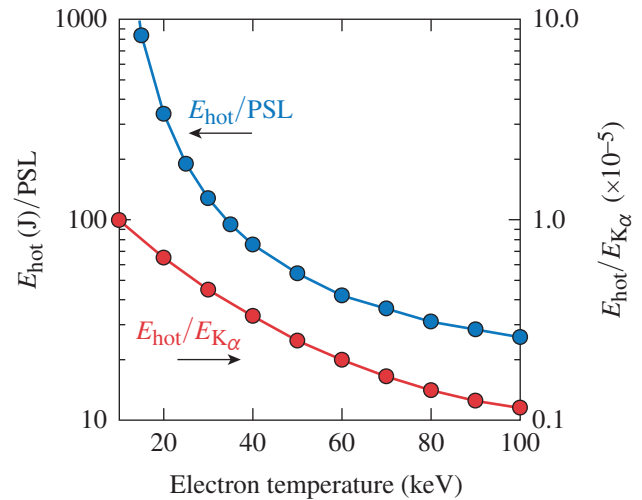
Figure 147.22
Curves used to determine the total energy in hot electrons for the two methods: using K_α and using continuum radiation. Shown are Monte Carlo calculations of the energy in hot electrons (E_{hot}) divided by either the measured Mo K_α energy per unit solid angle in the target normal direction (for targets containing a 30-μm-thick Mo layer) or the photostimulated luminescence (PSL) signal (for thick CH targets) registered by the fifth channel of the hard x-ray image-plate (HXIP) diagnostic. The inverse of these curves is simply the x-ray yield per energy in hot electrons. The x-ray energy is converted to PSL units using the known absolute calibration of the image plates.

lated luminescence unit (PSL) for channel 5 of the HXIP (see the next section). Using the intermediate channel 5 avoids the effect of thermal (or plasma) radiation on the lower channels, as well as the noise effect on the higher channels. Because of the good agreement of simulated and measured channel signals (see **Image-Plate–Based HXR Spectrometer**, p. 136), the same result would have been obtained with any other intermediate channel. The curves fall with increasing electron temperature because the radiation yields increase with T_{hot} [the curves rise at temperatures above ~100 keV (not shown in Fig. 147.22)]. Figure 147.22 can be used to determine E_{hot} (provided T_{hot} is known) because the x-ray yields for both the crystal x-ray spectrometer (XRS),[1] used to measure the Mo K_α line, and the image plates[8] are absolutely calibrated. The sharper fall of the HXIP (blue) curve was shown to be mitigated when the thermal radiation was included in the analysis (see **The Fraction of Laser Energy Converted to Hot Electrons**, p. 140). The blue curve in Fig. 147.22 assumes a 125-μm-thick CH target; the red curve is for a 30-μm-thick CH coating over 30-μm-thick Mo. If the HXIP is used with a target containing a high-Z layer, the HXR is emitted primarily by the high-Z material and the blue curve will be lower by a factor Z since the HXR yield from a

thick target is proportional to Z.[12] For low hot-electron temperatures, the thermal plasma emission (which is not calculated by the Monte Carlo code) is not negligible with respect to the hot-electron bremsstrahlung. Therefore, the measured radiation must be corrected before applying the blue curve in Fig. 147.22 (discussed in **The Fraction of Laser Energy Converted to Hot Electrons**, p. 140).

Using planar targets has an advantage over spherical targets: the density scale length $\left[\equiv (1/n \, dn/dx)^{-1}\right]$ in these experiments (for the highest intensity) was ~400 μm (from 2-D hydrodynamic simulations of the experiments).[1] For a given laser irradiance, the laser energy required to generate a long-scale-length plasma is smaller for planar targets than for spherical targets.[13,14]

Image-Plate–Based HXR Spectrometer

The hot-electron temperature was measured by a nine-channel instrument (HXIP) using an image plate as a detector. Image plates[8] contain an x-ray–sensitive layer of phosphor BaF(Br,I):Eu^{2+}. Recorded data are read in the photostimulated luminescence (PSL) process. The sensitivity of image plates was shown to be linear over five orders of magnitude in intensity.[15] The HXIP is contained in a 3/4-in.-thick lead enclosure to reduce background radiation from other radiation sources in the vacuum tank, including scattered target radiation. Additionally, the inside faces of the lead were covered, sequentially, by copper, aluminum, and Mylar layers to attenuate fluorescence from the walls. The spectral decomposition of the target radiation is achieved by an array of nine filters (aluminum and copper of different thicknesses) placed halfway between the target and the image-plate detector, with a total distance between the target and the image plate of 49 cm. Figure 147.23 shows the x-ray transmission curves of the nine filters. Figure 147.24 shows a typical image obtained on the HXIP. A single image plate records the nine projections through the filters (the signals) as well as the background. The background measured outside the nine squares is a result of Compton scattering of target radiation from the components within the HXIP enclosure and fluorescence from these components (primarily the lead walls). An additional background is caused by smearing (or bleeding) from the IP laser scanning. One advantage of using an IP-based system is that the total background is recorded and can be subtracted from the signals. The background is significant for only the last few channels (i.e., highest photon energy). For the first few channels the relative background intensity is <1%, for the intermediate channels it is <5%, and for the last channels it is ~50% of the signals. Therefore, knowing the background is essential to determining a reliable temperature. If the background is not fully subtracted, the inferred temperature will be

too high. One indication that the 2-D background subtraction is valid is that the resulting net signals are uniform over the square area of even the last channels.

The wall layers behind and close to the IP are one source of background radiation that requires special attention. Radiation that traverses the IP is absorbed into the back wall and scattered; fluorescent radiation enters the IP from its back. Monte Carlo
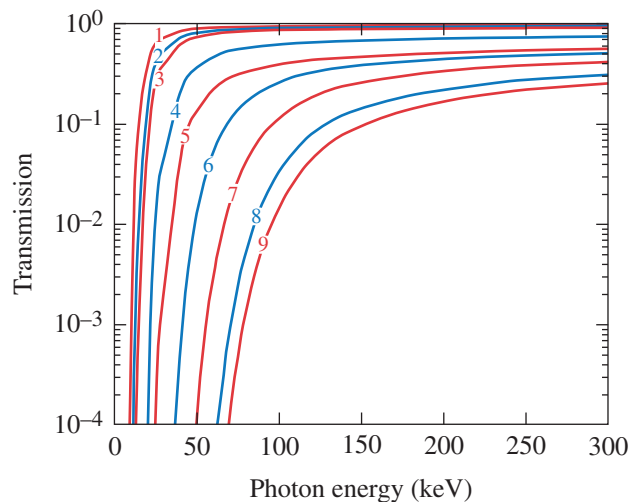
TC12828JR

Figure 147.23
X-ray transmission of HXIP channels 1 to 9 (left to right) as a function of the photon energy. Higher-number channels are sensitive to progressively higher photon energies.
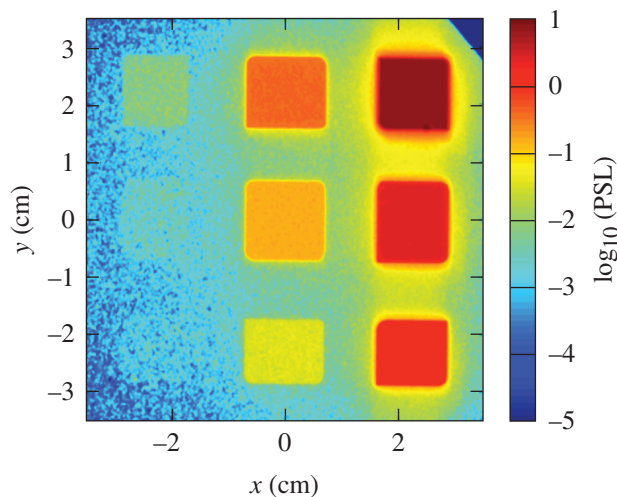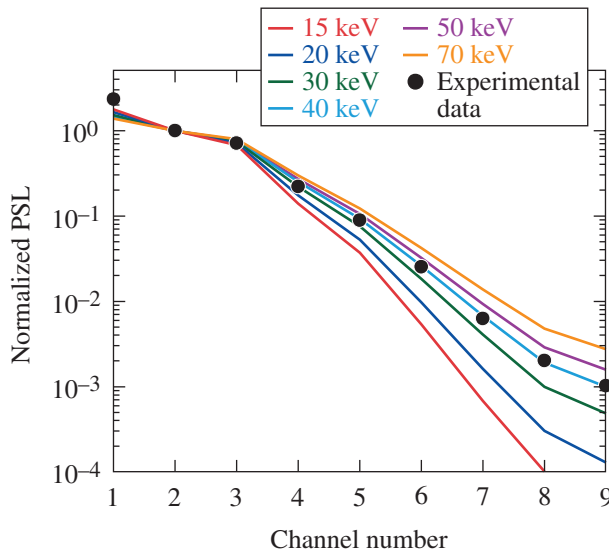

TC12829JR

Figure 147.24
A typical image (logarithmic intensity scale) obtained on an HXIP. The signals from nine channels are seen, as well as a background around and between the signals. The ability to subtract the background around each channel image makes it possible to correctly determine the emitted spectrum.

simulations show that the back-wall radiation is not uniform over the scale of the signal size (15 mm × 15 mm) because of the proximity; however, its intensity is about 20× lower than the total signal for any of the channels and is therefore unimportant.

Since the scattered radiation is removed from the net signals, they reflect only the transmission through the filters, which can be calculated without a Monte Carlo simulation. Figure 147.25 shows the calculated response curves for several hot-electron temperatures. The target HXR radiation spectrum is assumed to be a single exponential of the temperature T_{hot}. The measurements at each channel agree well with the best-fit curve, suggesting that the exponential assumption is valid. Therefore, in calculating the energy in hot electrons from Fig. 147.22, any channel (above the first) should give the same result. The signal curve relating to the HXIP in Fig. 147.22 corresponds to channel 5. This channel was chosen because lower channels are burdened by the plasma thermal radiation and by bound-free absorption in high-Z layers; also, higher channels may be too weak for reliable measurement. The filters for channel 5 absorb strongly below ~20 keV; this is the reason for the steep drop in the HXIP curve in Fig. 147.22. A special case is the first channel, which includes the radiation tail from the thermal plasma. This is why we normalized the curves and the data points to the second (rather than the first) channel.
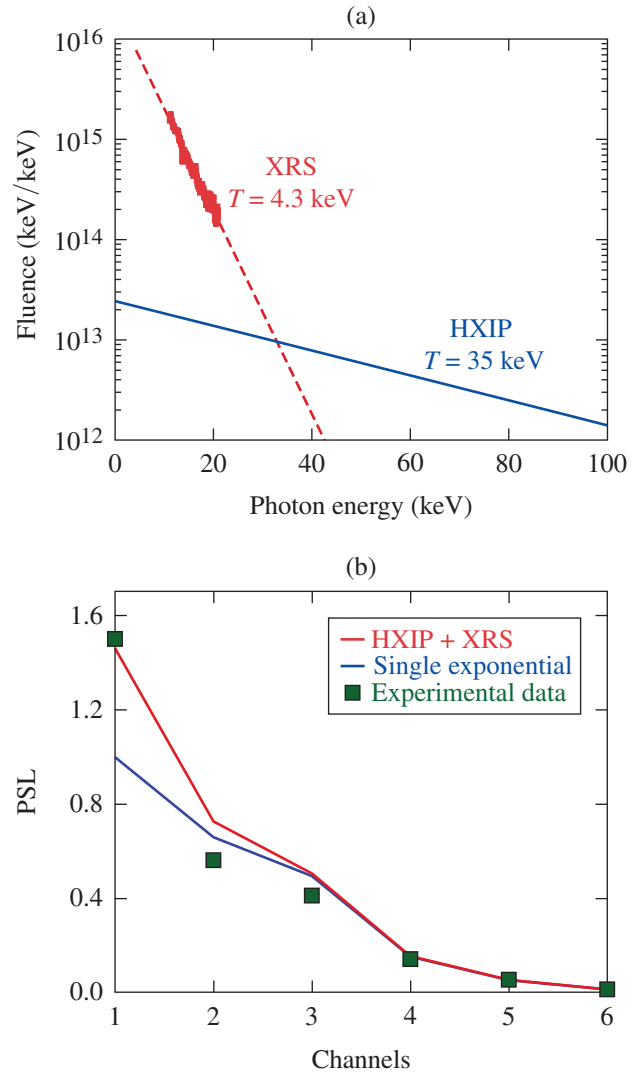
To demonstrate the role of the thermal radiation, Fig. 147.26(a) shows the simultaneous HXR spectrum deduced from the HXIP and the tail of the thermal spectrum measured using XRS. The irradiance for this shot was 6×10^{14} W/cm². The HXIP spectrum (which was assumed to be exponential) was obtained using the temperature from Fig. 147.25 and was normalized to the measured channel 5 signal. The target in Fig. 147.26 was CH; for a target with a higher-Z layer, the intensity of the induced component in Fig. 147.26(a) would be higher by about a fac-
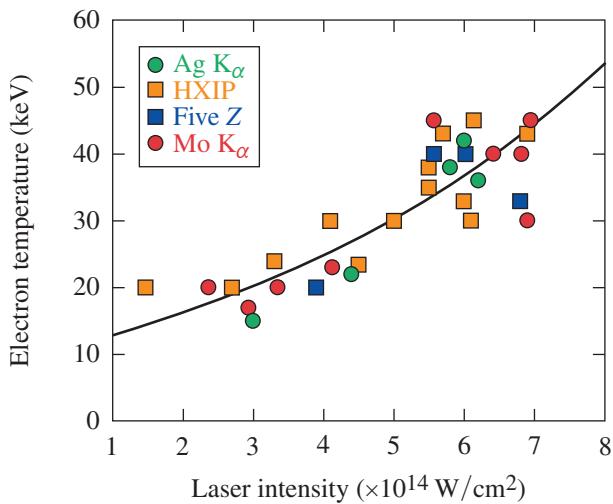

Figure 147.25
A typical example of determining hot-electron temperature using the HXIP data. The curves represent the nine-channel data, calculated by using the filter transmissions and measured image-plate (IP) sensitivity. To determine the hot-electron temperature, the curves of PSL data were normalized to the channel 2 data. Channel 1's excess signal is explained by the plasma thermal emission.

Figure 147.26
(a) The tail of the plasma-emission spectrum measured by the x-ray spectrometer (XRS) diagnostic (red line) and the hard x-ray (HXR) radiation emitted by hot electrons, as deduced from the HXIP measurement (blue line). (b) Using the sum of the two spectra in (a) as the input spectrum, the simulated channel signals (red curve) reproduce the measured HXIP data, including channel 1 (solid green squares), unlike the single-exponential spectrum (blue curve).

tor of Z, while the thermal plasma radiation would not change since the laser interaction in all cases is in the CH coating. Figure 147.26 illustrates that using HXIP alone to deduce the hot-electron temperature is valid if the first channel is excluded from the fitting procedure. Figure 147.26(b) shows the result of replacing the assumed single HXR exponential with the sum of the two exponentials in Fig. 147.26(a). The inclusion of the thermal spectrum with the calculated HXIP data agrees with the measured points for all channels, including channel 1. Figure 147.26(a) also shows that for low T_{hot} (<30 keV), the two spectra must be untangled (discussed in **The Fraction of Laser Energy Converted to Hot Electrons**, p. 140). For most fusion experiments, the relevant temperature is much higher and the low-temperature case is of interest only for exploring the TPD instability threshold. Figure 147.27 shows the compilation of temperature measurements from different shots as a function of the laser intensity. The temperatures inferred using HXIP measurements are represented by the orange squares. The other points in Fig. 147.27 are discussed in the next section.

TC12832JR

Figure 147.27
Compilation of measured hot-electron temperatures. The curve serves to guide the eye.

K_α Measurement of T_{hot}

Because of the discrepancy in temperature obtained by the HXRD (see Fig. 8 of Ref. 1) and HXIP, we designed three experiments to measure T_{hot} in a way that does not depend on the continuum radiation. Figure 147.28 shows the target configuration for the three experiments.

1. Thick Molybdenum Target

The target in this experiment consisted of 100-μm-thick molybdenum, coated with 30 μm of CH on both sides. The Mo
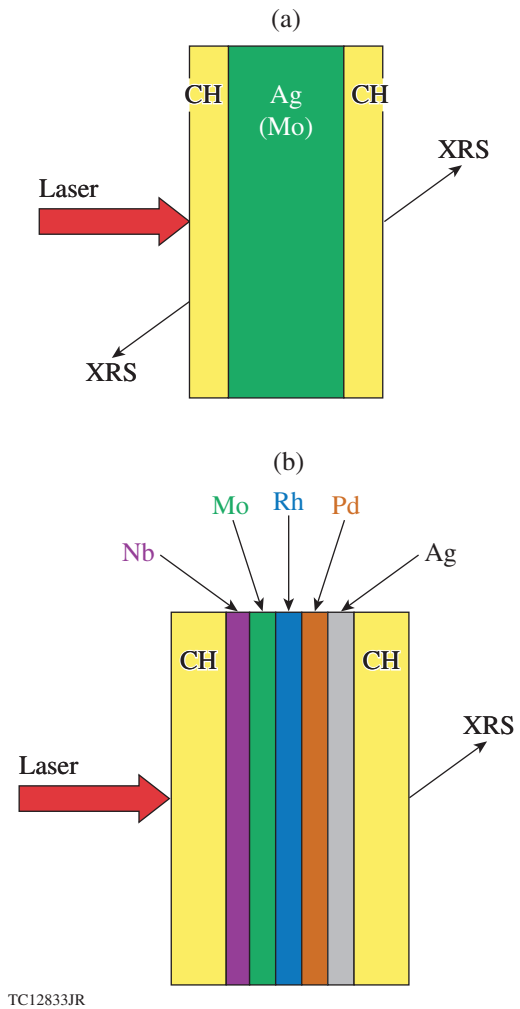

TC12833JR

Figure 147.28
Target configurations for three experiments designed to measure the hot-electron temperature using K_α emission from high-Z targets (not drawn to scale): (a) Thick molybdenum and silver targets. The targets consist of 100-μm-thick molybdenum (127-μm-thick silver), coated with 30 μm of CH on both sides. The measured quantities are the ratios of K_α emission from the front and rear of the target. (b) Five-element target. The target consists of five layers (Nb, Mo, Rh, Pd, and Ag), 5 μm thick each, coated with 30 μm of CH on both sides. The measured quantity is the K_α for increasing-Z elements.

thickness was larger than the range for most hot electrons, so the Mo K_α line was attenuated while traveling to the back of the target. For lower hot-electron temperatures, the K_α is emitted closer to the front surface, consequently being absorbed more when exiting from the back. Therefore, the ratio of the Mo K_α yields from the front and back of the target decreases with increasing T_{hot}. The ratio as a function of T_{hot} is calculated by the Monte Carlo code and shown in Fig. 147.29(a). The directions of the angles are with respect to the target normal. In the experiment, the laser intensity was varied and the calculated
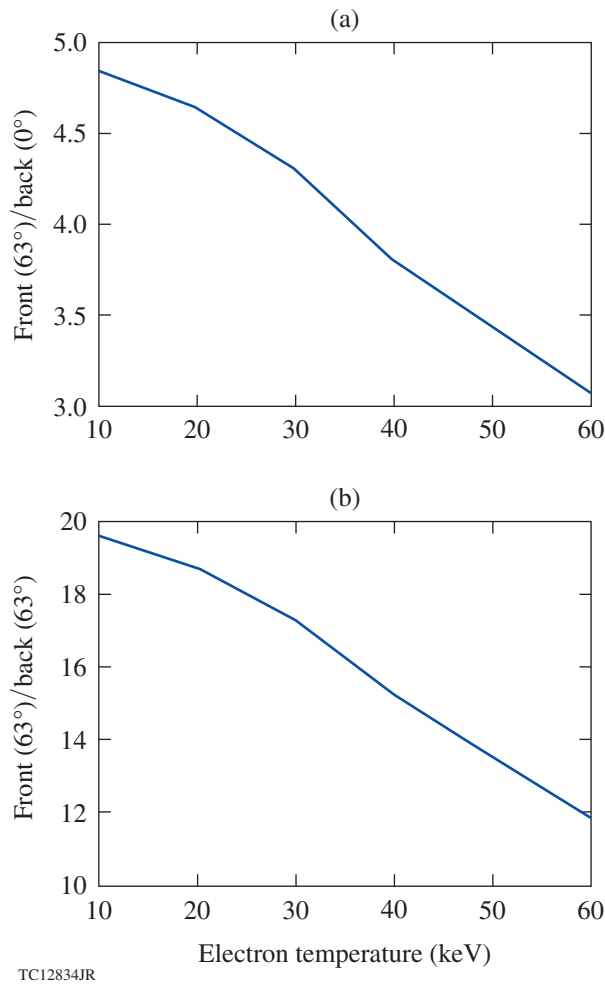
Figure 147.29
The ratios of Mo K_α and Ag K_α yields from the front and of the thick (a) Mo and (b) Ag targets, in the direction toward the detectors, as functions of the hot-electron temperature, calculated by the Monte Carlo code. The direction angles are with respect to target normal.

ratio was used to determine the hot-electron temperature. The resulting temperatures are shown by the solid red circles in Fig. 147.27.

2. Thick Silver Target

A 127-μm-thick silver layer replaced the molybdenum layer in the previous experiment. The Monte Carlo-calculated ratio of the Ag K_α yields from the front and back of the target is shown in Fig. 147.29(b). The higher K edge of Ag (25 keV) as compared with Mo (20 keV) reduces the fraction of coronal radiation available for K_α excitation and, therefore, supports ruling it out as a significant contributor to the observed K_α line (further discussed later in this section). The temperature results obtained are shown by the solid green circles in Fig. 147.27.

3. Five-Element Target

This target consists of five layers (Nb, Mo, Rh, Pd, and Ag), 5 μm thick each, coated with 30 μm CH [Fig. 147.28(b)]. The five corresponding K_α lines are measured using XRS behind the target. The five layers are of increasing Z in the direction of the incident laser (Z = 41, 42, 45, 46, 47). Each K_α line of a given Z can excite the K_α lines of the lower-Z layers but not of the higher-Z layers. The main effect is the decrease in the number of hot electrons as they move in the direction of the laser. Therefore, the XRS at the back of the target measures five K_α lines of decreasing intensity for increasing Z (see Fig. 147.30). This decrease is slower for a higher hot-electron temperature. The Monte Carlo code simulations of hot-election transport through this target are used to derive T_{hot} from the rate of K_α intensity drop as a function of Z (see Fig. 147.31). The resulting temperatures are shown by the solid blue squares in Fig. 147.27.
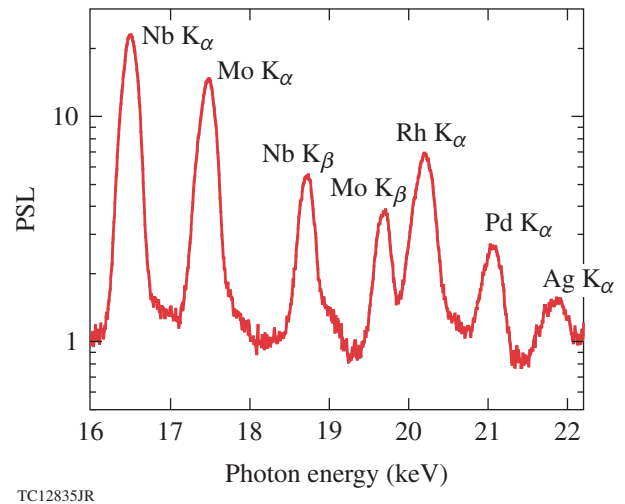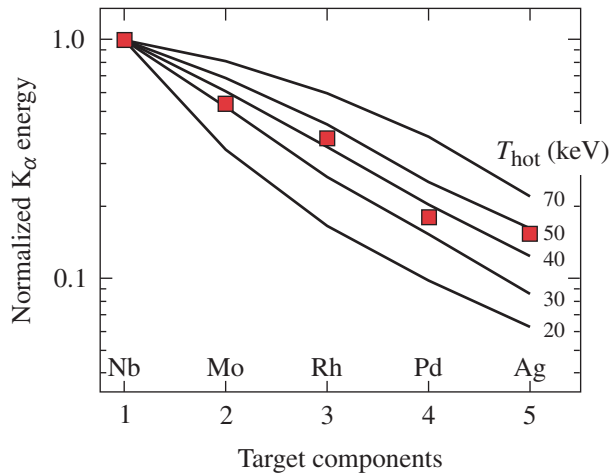

Figure 147.30
An example of the x-ray spectrum from a five-element target, as measured by XRS. The K_α lines are used to determine the hot-electron temperature.

In addition to hot electrons, K_α lines can also be excited by radiation, both thermal radiation from the plasma and bremsstrahlung radiated by the hot electrons. Only the latter, however, is accounted for in the Monte Carlo simulations. Therefore, plasma radiation's contribution to the K_α intensity must be shown to be negligible. A clear indication that the K_α lines in our experiments are excited primarily by hot electrons and their radiation and not by plasma radiation is seen in the laser-intensity dependence of the K_α lines. Figure 6 of Ref. 1 shows that for a rise in the laser intensity by a factor of ~2, the Mo K_α intensity rises by almost a factor of 10^4 (see also the related Fig. 147.34 below). On the other hand, the plasma
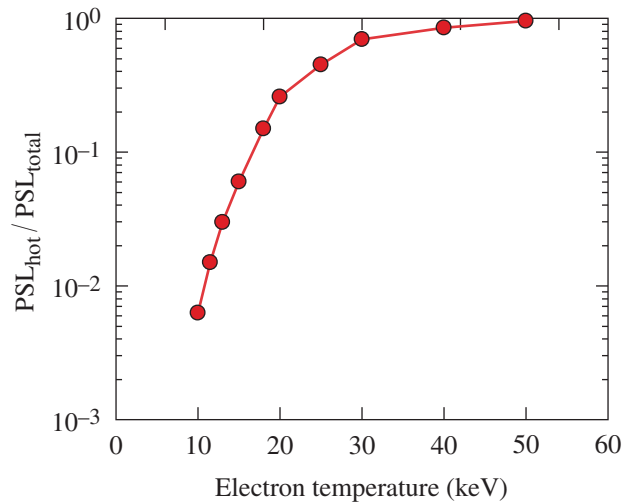
TC12836JR

Figure 147.31

Monte Carlo curves of K_α intensity for the five elements in the target, normalized to the first element. The data (for a laser irradiance of 6×10^{14} W/cm^2) indicate $T_{hot} \sim 40$ keV.


TC12837JR

Figure 147.32

Relative contribution of the plasma electrons and the hot electrons to the measured total x-ray spectrum. Experimental curves such as the two curves shown in Fig. 147.26(a), for various laser intensities, are convolved with the HXIP sensitivity of channel 5; plotted is the ratio of the signal caused by hot electrons alone and that caused by the hot electrons plus the plasma radiation. As the hot-electron temperature drops, so does the relative contribution of hot-electron radiation to the total measured x-ray yield.

continuum intensity increases about linearly with the laser intensity, indicating that its contribution to the K_α excitation is negligible. An additional indication of the ratio between the two radiations in a pure CH target is seen in Fig. 147.26(a). For T_{hot} higher than ~20 keV, the hot-electron curve rises sharply (because of increased hot-electron production at higher intensities) and the continuum above the K edge of, say, Ag (25 keV) will be dominated by the hot-electron bremsstrahlung.

The Fraction of Laser Energy Converted to Hot Electrons

As seen in Fig. 147.26(a), the total measured x-ray yield includes a contribution from the thermal-plasma radiation, which is not included in the Monte Carlo code calculations. Therefore, the measured radiation should be corrected (reduced) before using the blue curve in Fig. 147.22 to deduce the energy in hot electrons. This correction is especially important at low hot-electron temperatures, where the hot-electron bremsstrahlung drops very fast. Figure 147.32 shows the correction factor; i.e., the ratio $R = PSL_{hot}/PSL_{total}$ of hot-electron–induced radiation and total radiation (including the thermal-plasma radiation), measured in channel 5, as a function of T_{hot}. The correction factor R is calculated using the measured composite x-ray spectra, like those of Fig. 147.26(a): the spectrum (with and without the plasma component) is multiplied by channel 5, filters transmission and the IP sensitivity, and then integrated over photon energies. This ratio can be approximated as $R = -0.521 + 4.81 \times 10^{-2} \times T_{hot} - 3.59 \times 10^{-4} \times T_{hot}^2$, where T_{hot} is in keV. The results are shown in Fig. 147.32.

Using the correction factor R, the HXIP curve in Fig. 147.22 can now be modified to allow for the contribution of the plasma radiation with the results shown in Fig. 147.33. The red curve is the corresponding blue curve from Fig. 147.22, shown as reference. To use this curve, the experimental radiation must be corrected for the plasma radiation. The blue curve in Fig. 147.33 was obtained by multiplying the red curve by the correction factor (Fig. 147.32). When using the blue curve in Fig. 147.33, the total measured channel 5 readings must be used (without subtracting the thermal contribution). The corrected curve indicates that the dependence of the hot-electron yield on hot-electron temperature is weak. Therefore, the discrepancy between the HXRD and HXIP temperature results (see the **Introduction**, p. 134) is not very important when calculating the energy in hot electrons; however, the penetration depth of hot electrons, relevant to preheat calculation, remains important.

To verify the validity of the present derivation of hot-electron energy, Fig. 147.34 compares the fraction of laser energy converted into hot electrons (f_{hot}) using the present HXIP results (blue circles) and previous Mo K_α results[1] (red circles). The HXIP results refer to 125-μm-thick CH targets, whereas the Mo K_α results refer to CH-coated Mo targets. The tempera-
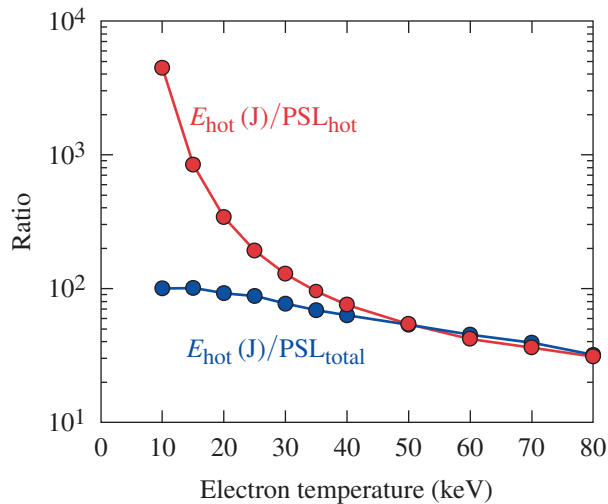
Figure 147.33
The blue curve in Fig. 147.22 is adjusted to include the contribution of the thermal radiation, using the results of Fig. 147.32. The red curve here reproduces the unadjusted Fig. 147.22 curve. Since that curve shows E_{hot}/PSL_{hot} and Fig. 147.32 shows the ratio PSL_{hot}/PSL_{total}, the product of these quantities is E_{hot}/PSL_{total} and is represented here by the blue curve. When the adjusted, measured channel 5 signal is used, the resulting E_{hot} is seen to depend only weakly on T_{hot}.
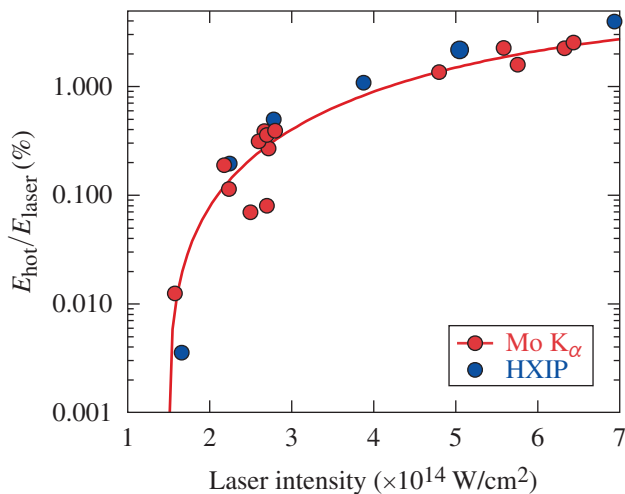
Figure 147.34
The fraction of total laser energy converted to energy in hot electrons. The red circles represent the data from Ref. 1, using the Mo K_α line from a CH-coated Mo target, with T_{hot} corrected based on the laser-intensity scaling found in the present experiments. The blue circles represent data from a 125-μm-thick CH target, using the HXR continuum measured by HXIP. The results indicate that these two methods of deducing E_{hot} are equivalent.

ture values in the older experiment were corrected using the scaling with laser intensity obtained in this experiment. The agreement shows that the method for measuring hot-electron energy using the HXIP (corrected for the thermal radiation) is consistent with the method in Ref. 1 using Mo K_α lines. The agreement also shows that the production of hot electrons in CH-coated Mo is very similar to that in thick CH targets. It should be noted that the large possible error in f_{hot} (because of the thermal contribution) near the threshold can be tolerated because of the steep rise, and that typical fusion implosion experiments correspond to the upper end of the intensity range in Fig. 147.34, where the thermal contribution is negligible.

Conclusion

This article extends our previous measurements[1–3] of the temperature and total energy of laser-generated hot electrons, using 2-ns UV pulses at 10^{14} W/cm^2 on the OMEGA EP laser.[1–3] The three-channel fluorescence-photomultiplier detector (HXRD) was replaced with a nine-channel image-plate–based detector (HXIP). For the same conditions, the measured temperatures are lower than those measured using a HXRD by a factor of ~1.5 to 1.7. This measurement was supplemented with three experiments that measured the hot-electron temperature using K_α emission from high-Z target layers. These experiments gave temperatures that were consistent with those measured using the HXIP. The lower hot-electron temperatures, however, do not significantly impact the deduced total energy in hot electrons when the effect of the thermal plasma radiation on bremsstrahlung measurements is taken into account.

Lower temperatures mean that the simulated preheat in cryogenic spherical implosions, using HXRD temperatures, could be overestimated, however, since lower T_{hot} entails smaller penetration into the target core. In fact, recent cryogenic experiments[16] show that the preheat is smaller than predicted (by measuring the degradation in areal density compared to the one predicted), and even the preheat remains small when the production of hot electrons increases significantly. This could be caused by reduced penetration of hot electrons into the core.

While the fraction of laser energy converted into hot electrons is found to increase up to 1% to 3% with the laser intensity, other factors can contribute to lowering the preheat of the cold dense shell in spherical implosions, such as a large angular divergence of the hot electrons.[17] High-Z ablators are capable of reducing the production of hot electrons because of a shorter scale length and a higher plasma temperature.[18]

REFERENCES

1. B. Yaakobi, P.-Y. Chang, A. A. Solodov, C. Stoeckl, D. H. Edgell, R. S. Craxton, S. X. Hu, J. F. Myatt, F. J. Marshall, W. Seka, and D. H. Froula, Phys. Plasmas **19**, 012704 (2012).

2. D. H. Froula, B. Yaakobi, S. X. Hu, P.-Y. Chang, R. S. Craxton, D. H. Edgell, R. Follett, D. T. Michel, J. F. Myatt, W. Seka, R. W. Short, A. Solodov, and C. Stoeckl, Phys. Rev. Lett. **108**, 165003 (2012).

3. D. H. Froula, D. T. Michel, I. V. Igumenshchev, S. X. Hu, B. Yaakobi, J. F. Myatt, D. H. Edgell, R. Follett, V. Yu. Glebov, V. N. Goncharov, T. J. Kessler, A. V. Maximov, P. B. Radha, T. C. Sangster, W. Seka, R. W. Short, A. A. Solodov, C. Sorce, and C. Stoeckl, Plasma Phys. Control. Fusion **54**, 124016 (2012).

4. J. D. Lindl, *Inertial Confinement Fusion: The Quest for Ignition and Energy Gain Using Indirect Drive* (Springer-Verlag, New York, 1998), Chap. 11.

5. *LLE Review Quarterly Report* **79**, 121, Laboratory for Laser Energetics, University of Rochester, Rochester, NY, LLE Document No. DOE/SF/19460-317, NTIS Order No. DE2002762802 (1999).

6. V. A. Smalyuk, D. Shvarts, R. Betti, J. A. Delettrez, D. H. Edgell, V. Yu. Glebov, V. N. Goncharov, R. L. McCrory, D. D. Meyerhofer, P. B. Radha, S. P. Regan, T. C. Sangster, W. Seka, S. Skupsky, C. Stoeckl, B. Yaakobi, J. A. Frenje, C. K. Li, R. D. Petrasso, and F. H. Séguin, Phys. Rev. Lett. **100**, 185005 (2008).

7. C. Stoeckl, V. Yu. Glebov, D. D. Meyerhofer, W. Seka, B. Yaakobi, R. P. J. Town, and J. D. Zuegel, Rev. Sci. Instrum. **72**, 1197 (2001).

8. A. L. Meadowcroft, C. D. Bentley, and E. N. Stott, Rev. Sci. Instrum. **79**, 113102 (2008).

9. A. R. Christopherson, R. Betti, W. Theobald, and J. Howard, "Probing Hot Electron Preheat and Hot Spot Asymmetries in ICF Implosions," the Ninth International Conference on Inertial Fusion Sciences and Applications (IFSA 2015), Seattle, WA, 20–25 September 2015 (Paper Th.O.2.2).

10. *LLE Review Quarterly Report* **125**, 37, Laboratory for Laser Energetics, University of Rochester, Rochester, NY, LLE Document No. DOE/NA/28302-993 (2010).

11. I. Kawrakow, Med. Phys. **27**, 485 (2000); I. Kawrakow, E. Mainegra-Hing, D. W. O. Rogers, F. Tessier, and B. R. B. Walters, "The EGSnrc Code System: Monte Carlo Simulation of Electron and Photon Transport," National Research Council Canada, Ottawa, Canada, NRCC Report PIRS-701 (May 2011).

12. K. A. Brueckner, Phys. Rev. Lett. **36**, 677 (1976); R. P. Drake, R. E. Turner, B. F. Lasinski, E. A. Williams, K. Estabrook, W. L. Kruer, E. M. Campbell, and T. W. Johnston, Phys. Rev. A **40**, 3219 (1989); T. Döppner *et al.*, Phys. Rev. Lett. **108**, 135006 (2012).

13. D. T. Michel, A. V. Maximov, R. W. Short, J. A. Delettrez, D. Edgell, S. X. Hu, I. V. Igumenshchev, J. F. Myatt, A. A. Solodov, C. Stoeckl, B. Yaakobi, and D. H. Froula, Phys. Plasmas **20**, 055703 (2013).

14. D. T. Michel, A. V. Maximov, R. W. Short, S. X. Hu, J. F. Myatt, W. Seka, A. A. Solodov, B. Yaakobi, and D. H. Froula, Phys. Rev. Lett. **109**, 155007 (2012).

15. J. Miyahara *et al.*, Nucl. Instrum. Methods Phys. Res. **A246**, 572 (1986).

16. V. N. Goncharov, T. C. Sangster, R. Betti, T. R. Boehly, M. J. Bonino, T. J. B. Collins, R. S. Craxton, J. A. Delettrez, D. H. Edgell, R. Epstein, R. K. Follet, C. J. Forrest, D. H. Froula, V. Yu. Glebov, D. R. Harding, R. J. Henchen, S. X. Hu, I. V. Igumenshchev, R. Janezic, J. H. Kelly, T. J. Kessler, T. Z. Kosc, S. J. Loucks, J. A. Marozas, F. J. Marshall, A. V. Maximov, R. L. McCrory, P. W. McKenty, D. D. Meyerhofer, D. T. Michel, J. F. Myatt, R. Nora, P. B. Radha, S. P. Regan, W. Seka, W. T. Shmayda, R. W. Short, A. Shvydky, S. Skupsky, C. Stoeckl, B. Yaakobi, J. A. Frenje, M. Gatu-Johnson, R. D. Petrasso, and D. T. Casey, Phys. Plasmas **21**, 056315 (2014).

17. B. Yaakobi, A. A. Solodov, J. F. Myatt, J. A. Delettrez, C. Stoeckl, and D. H. Froula, Phys. Plasmas **20**, 092706 (2013).

18. R. K. Follett, J. A. Delettrez, D. H. Edgell, V. N. Goncharov, R. J. Henchen, J. Katz, D. T. Michel, J. F. Myatt, J. Shaw, A. A. Solodov, C. Stoeckl, B. Yaakobi, and D. H. Froula, Phys. Rev. Lett. **116**, 155002 (2016).